Electronic Supplementary Material (ESI) for New Journal of Chemistry.

Supplementary data for

A Universal and Controllable Strategy of Constructing Transition-Metal Nitride Heterostructure for Highly Enhanced Bifunctional Electrocatalysis

Bin Chang,[a] *Yueyao Zhong,*[a] *Zizheng Ai,*[a] *Jiaqi Zhang,*[c] *Dong Shi,*[a] *Kang Zhang,*[a] *Yongliang Shao,*[a] *Jianxing Shen,*[b] *Baibiao Huang,*[a] *Lei Zhang,*[a]***Yongzhong Wu*[a] *and Xiaopeng Hao*[a]

[a] State Key Lab of Crystal Materials, Shandong University, Jinan, 250100, P. R. China

[b] Department of Materials Science and Engineering, Qilu University of Technology (Shandong Academy of Science), Jinan, 250353, P. R. China

[c] Shandong Experimental High School

*E-mail: leizhang528@sdu.edu.cn

This file includes:

S1. Materials

S2. Characterization Methods

S3. Electrochemical Tests

S4. Supplementary Figures S1–S15

S5. Supplementary Table S1–S2

S1. Materials

Nickel nitrate hexahydrate ($Ni(NO_3)_2{\cdot}6H_2O$), cobalt nitrate hexahydrate ($Co(NO_3)_2{\cdot}6H_2O$), copper nitrate ($Cu(NO_3)_2$), ammonium molybdate ($(NH_4)_6Mo_7O_{24}$), dodecyl trimethyl ammonium bromide (DTAB), ethanediol and nickel foam were purchased from Sinopharm Chemical Reagent Co. Ltd. Pt/C (20 wt% Pt on Vulcan XC-72R) and RuO_2 was purchased from Alfa Aesar. Nafion (20 wt%) was purchased from Sigma-Aldrich. All chemicals were of analytical reagent grade and used as received without further purification. Solutions were freshly prepared with deionized water.

S2. Characterization Methods

X-ray diffraction (XRD) patterns of the materials were acquired on a diffractometer (Bruker D8) using a Cu Kα radiation source (λ =1.5418 Å) with a 2θ scan from 15^o to 85^o with a step size of 0.04. X-ray photoelectron spectroscopy (XPS) measurements of all materials were performed on a Thermo ESCALAB 250 X-ray photoelectron spectrometer using mono chromated Al K radiation (1486.8 eV). All the binding energies were calibrated to the C 1s peak at 284.6 eV of the surface adventitious carbon. Scanning electron microscopy (SEM) images were obtained with a Hitachi S-4800 field-emission scanning electron microscope. High-resolution TEM (HRTEM) images were obtained using a Philips Tecnai 20U-Twin microscope at an acceleration voltage of 200 kV. The solution of samples was achieved after 30 min ultrasonic pretreatment. The TEM samples were prepared by dropping the primed solution onto a copper grid with polyvinyl formal support film and dried in air.

S3. Electrochemical Tests

Commercial Pt/C or RuO_2 loaded on nickel foam were prepared for comparison, respectively. Pt/C powder (10 mg) and RuO_2 powder (10 mg) were firstly dispersed into 980 μL of water/ethanol (v/v=1:4) solvent containing 20 μL of 20 wt% Nafion and sonicated for 1 h. Then, 100 μL of the Pt/C ink and RuO_2 ink were loaded on nickel foam (1×2.5 cm^2) with Pt/C and RuO_2 loading 0.4 mg cm^{-2} for activity test. Prior to measurement, a resistance test was made and the iR compensation was applied to all initial data for further analysis. Electrochemical impedance spectroscopy (EIS) was carried out in potentiostatic mode from 10^5 to 0.01 Hz. Polarization curves of hydrogen or oxygen generation were obtained using linear sweep voltammetry (LSV) with scan rate of 2 mV·s^{-1} at 25 °C in the aqueous solutions (0.5 M H_2SO_4 or 1.0 M KOH) with constant N_2 (g) continually purging for 30 min prior to the measurements. All the polarization curves are steady-state ones after several cycles. In all measurements, the Ag/AgCl reference electrode was calibrated with respect to the reversible hydrogen electrode (RHE). The potentials of HER/OER measurement were converted to RHE using the equation given by $E_{RHE} = E_{Ag/AgCl} + 0.0591 \times pH + 0.194$, resulting in a shift of -0.2117 V versus RHE in acidic solution (0.5 M H_2SO_4, pH~0.3) and +1.0155V versus RHE in alkaline solution (1.0 M KOH, pH~13.9), respectively. The long-term stability test was carried out using chronopotentiometric measurements. The electrochemical stability of the catalyst was also evaluated by cycling the electrodes for 5000 times. Overall water splitting was performed in a two-electrode system. One Ni_3N@NiMoN-Ni foam electrode acted as the positive electrode for OER and the other Ni_3N@NiMoN-Ni foam was used as the negative electrode for HER.

S4. Supplementary Figures

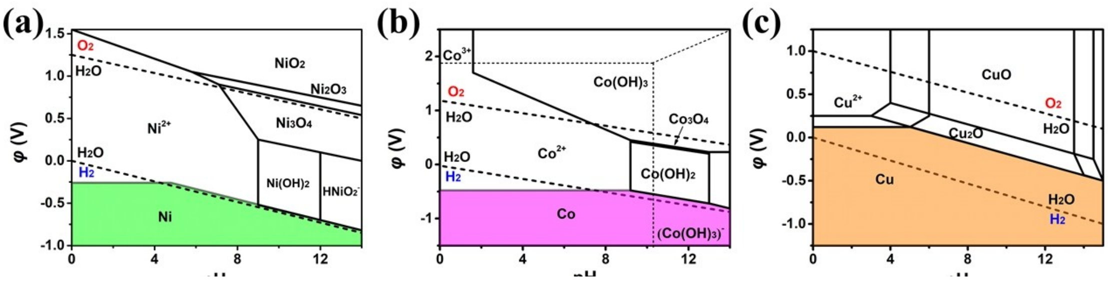

Figure S1. Pourbaix diagram of nickel electrodeposition (a), cobalt electrodeposition (b) and copper electrodeposition (c).

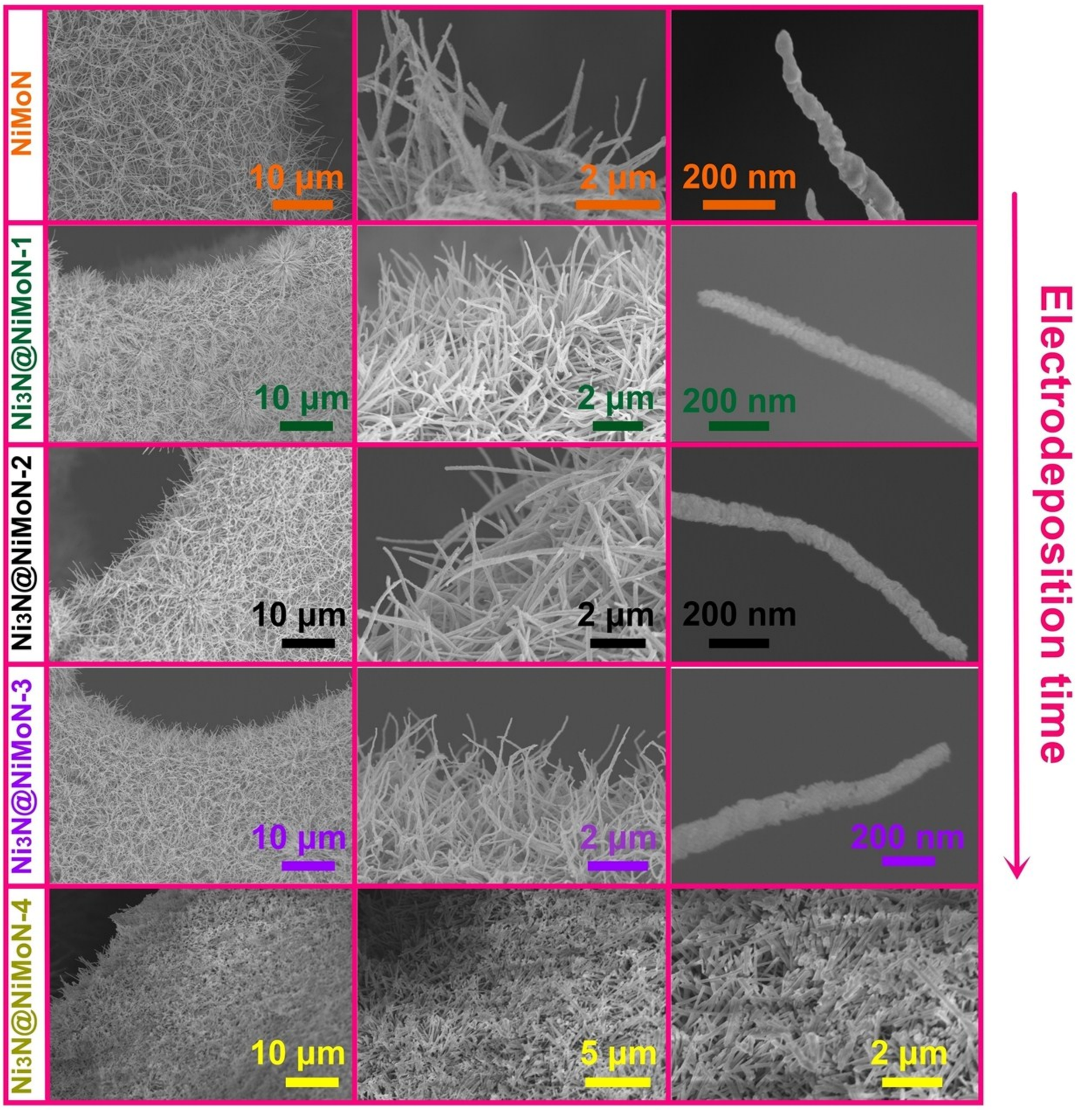

Figure S2. SEM images of the Ni_3N@NiMoN sample with different electrodeposition time of 0, 100, 200, 300 and 400 s, which were named as NiMoN and Ni_3N@NiMoN-1/2/3/4, respectively.

The morphology of the material synthesized with suitable electrodeposition time is uniform. Comparing to bare NiMoN, the surface of Ni_3N@NiMoN-1/2/3 become rough (**Figure S2**). However, the morphology of Ni_3N@NiMoN-4 become uneven and mussy with over electrodeposition time.

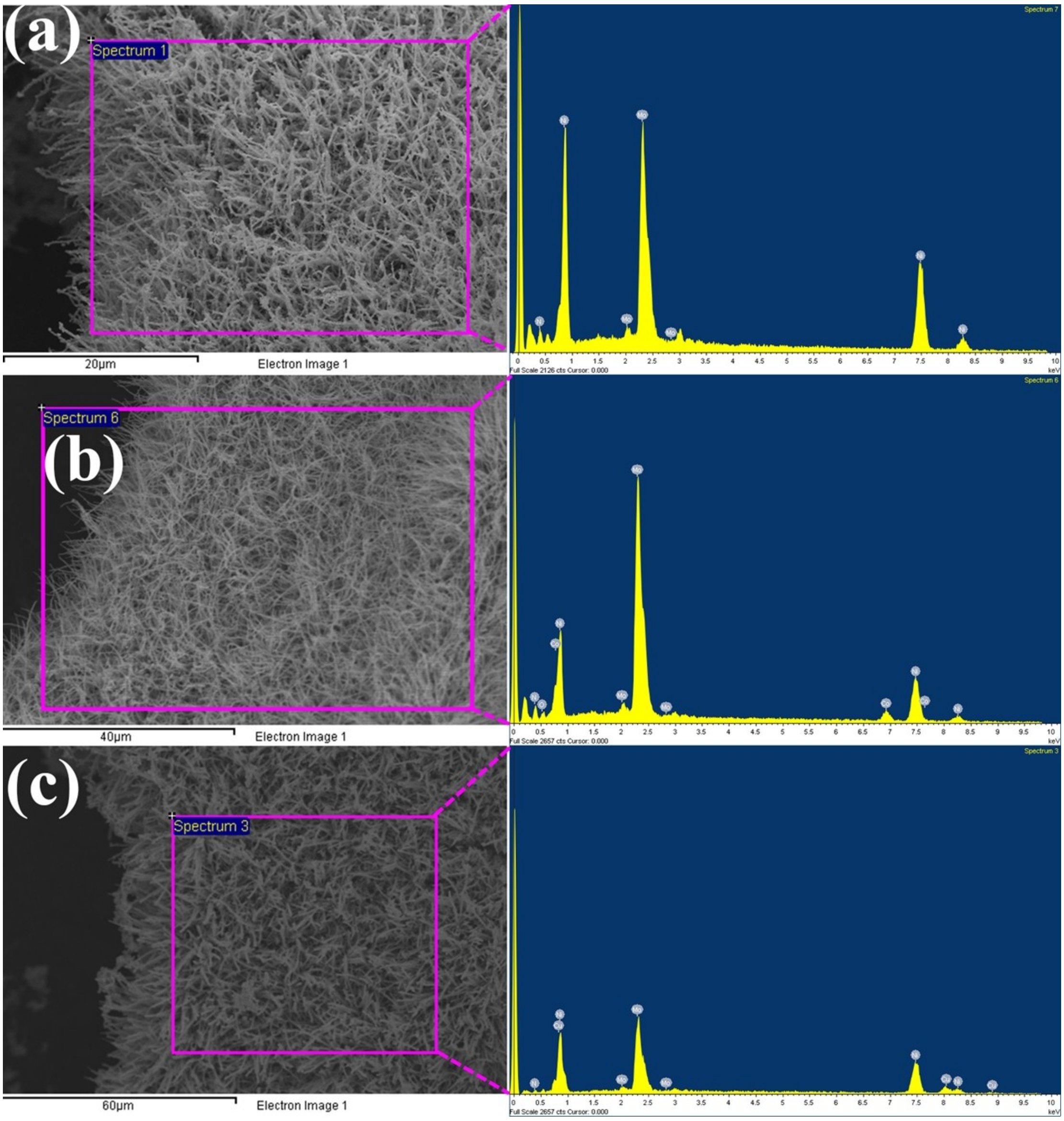

Figure S3. EDS patterns images of the as-prepared Ni_3N@NiMoN (a), Co_4N@NiMoN (b), and Cu_3N@NiMoN (c).

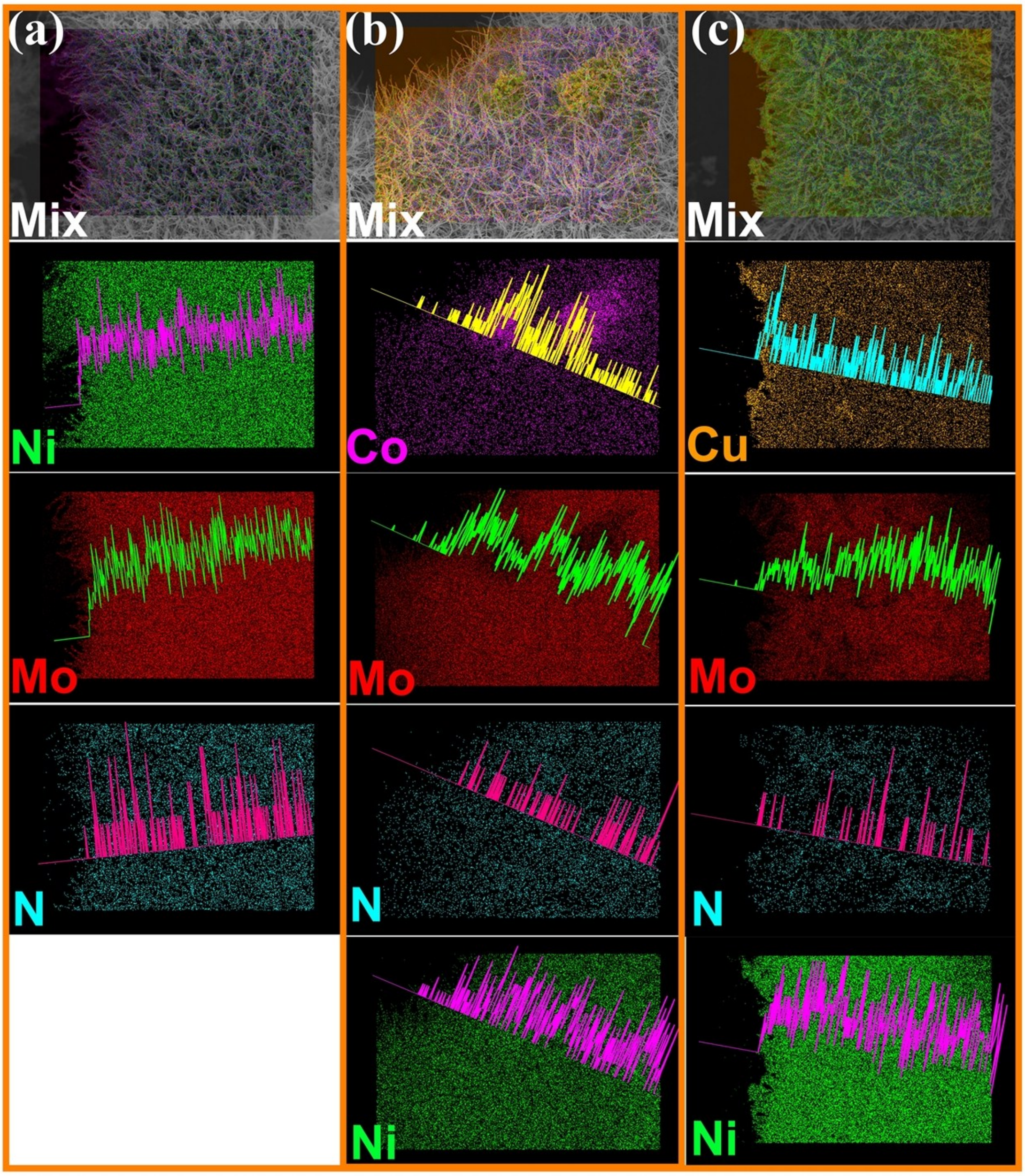

Figure S4. Elemental mapping images of the as-prepared Ni_3N@NiMoN (a), Co_4N@NiMoN (b), and Cu_3N@NiMoN (c).

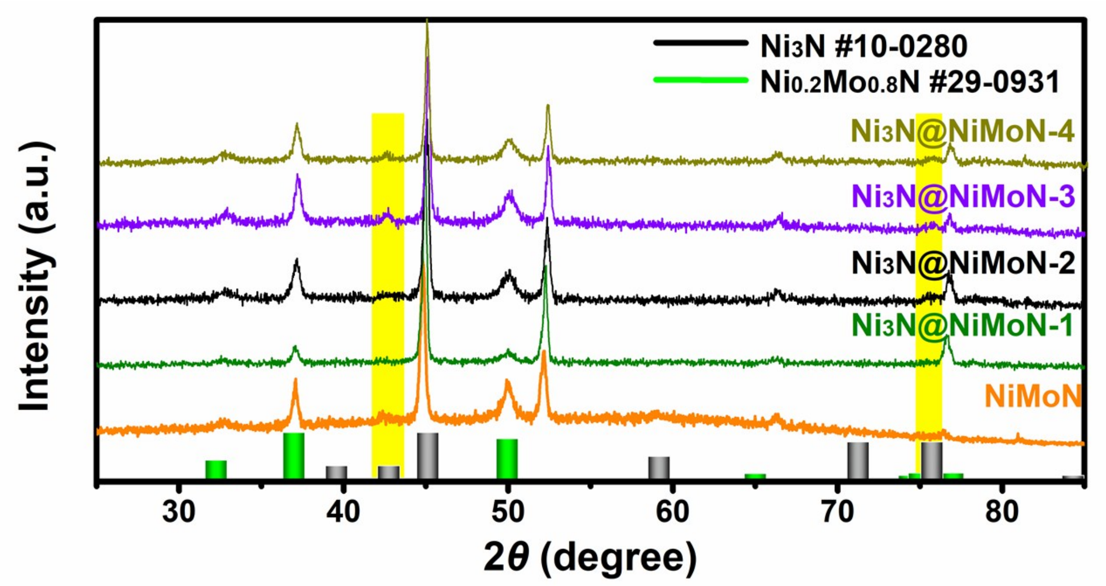

Figure S5. XRD patterns of the as-synthesized NiMoN, and Ni_3N@NiMoN1/2/3/4.

Typical strong peaks at approximately 44.5°, 51.8° and 76.3° are observed in all XRD patterns and correspond to the nickel foam **(Figures S5**).

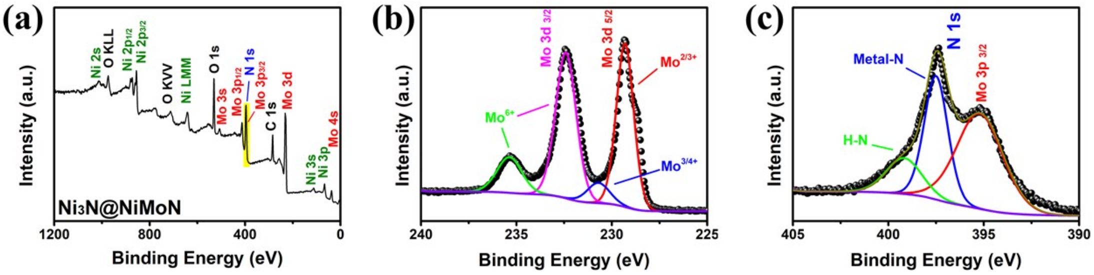

Figure S6. The wide scan XPS spectra of Ni_3N@NiMoN (a). High-resolution XPS spectra in Mo 3d region (b) and N 1s region (c) for the as-synthesized Ni_3N@NiMoN.

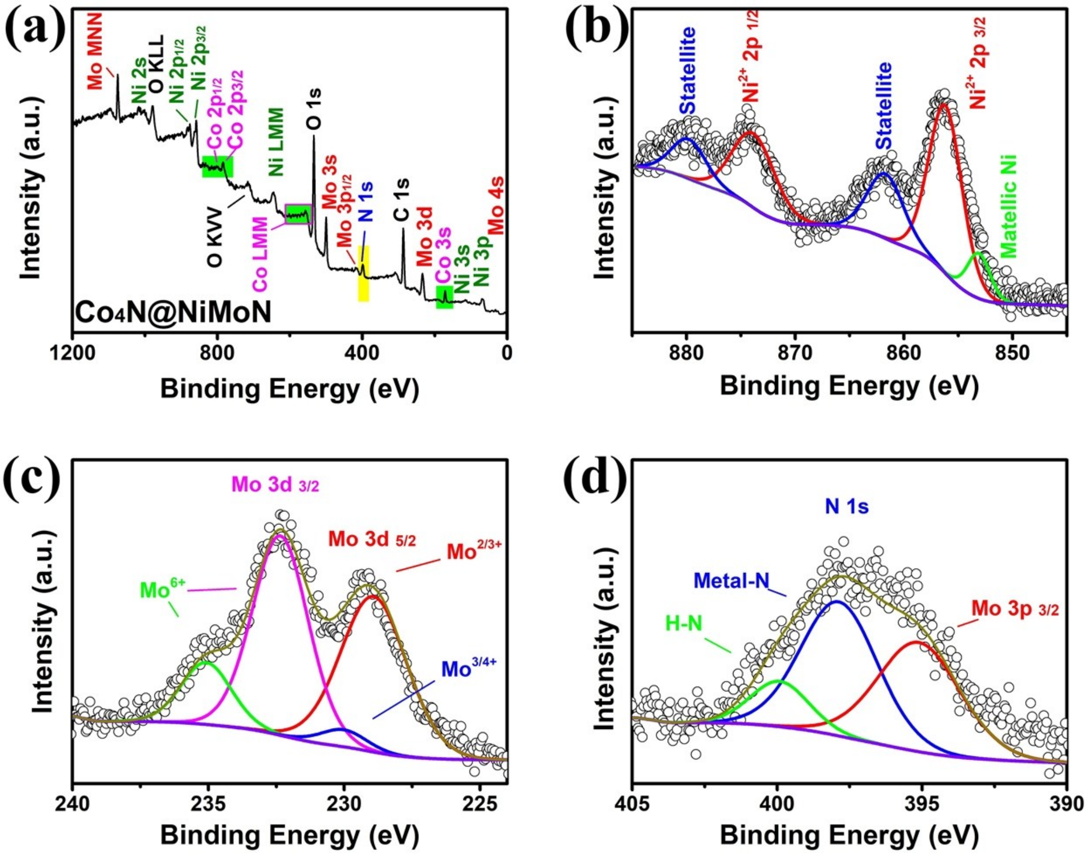

Figure S7. The wide scan XPS spectra of Co$_4$N@NiMoN (a). High-resolution XPS spectra in Ni 2p region (b), Mo 3d region (c) and N 1s region (d) for the as-synthesized Co$_4$N@NiMoN.

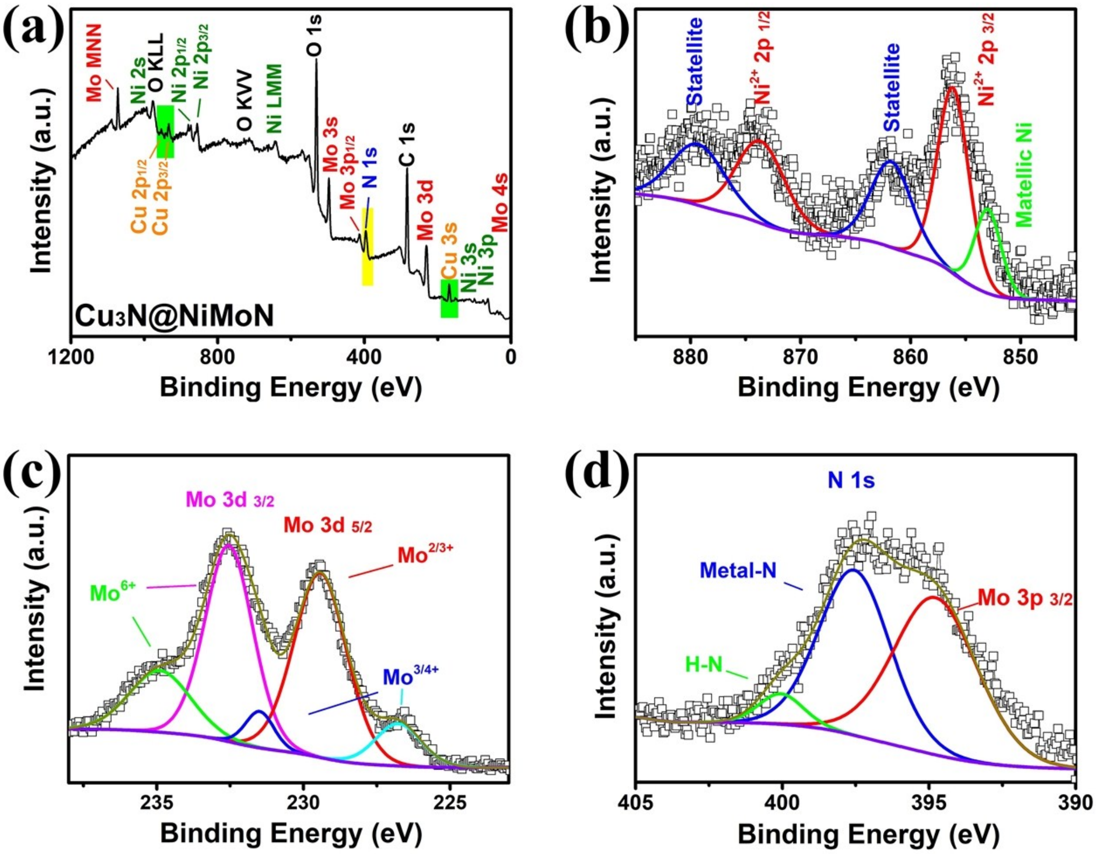

Figure S8. The wide scan XPS spectra of Cu_3N@NiMoN (a). High-resolution XPS spectra in Ni 2p region (b), Mo 3d region (c) and N 1s region (d) for the as-synthesized Cu_3N@NiMoN.

In the Ni 2p XPS spectra displayed in **Figures S7b and 8b**, typical peaks for Ni ions are described as $Ni_{0.2}Mo_{0.8}N$ and the additional peak at 852.5 eV can be assigned to metallic nickel.[1,2] For the spectrum of the Mo 3d (**Figure S6b**), two peaks with the binding energy of 229.0 eV and 232.4 eV are attributed to Mo 3d5/2 and Mo 3d3/2 of Mo^{6+}. Fitting data reveal three Mo species in **Figure S6b**: $Mo^{2/3+}$(the binding energy at 229.1 eV), $Mo^{3/4+}$(the binding energy at 230.8 eV), and Mo^{6+}(the binding energy at 232.5 and 235.4 eV) for Mo on the surface of $Ni_{0.2}Mo_{0.8}N$. In the N 1s spectrum (**Figure S6c**), it is clearly seen that N 1s and Mo 3p3/2 have partial overlap. The peak at 397.6 eV corresponds to N 1s which can be assigned to a characteristic peak for metal nitrides, revealing that N atoms are combined with the Ni/Mo surface of Ni_3N@$Ni_{0.2}Mo_{0.8}N$. The additional small N 1s peak at 399.2 eV is attributed to the N-H species, which suggests that there are abundant H species on the surface of the structures.[1] The similar characteristic peaks of Mo and N are also presented in the spectra of Co_4N@NiMoN and Cu_3N@NiMoN (**Figures S7c,d and S8c,d**).[3-6] Ni_3N@NiMoN perfectly exemplifies the advantages of transition metal nitrides heterostructures for electrocatalysis. The Ni^+ and Ni-N bond in the metal nitride are thought to be active for OER, and the presence of $Mo^{3/4+}$ and Mo^{6+} species due to the surface oxidization of $Mo^{2/3+}$ upon air exposure is also conducive to electerocatalytic HER. [1,2]

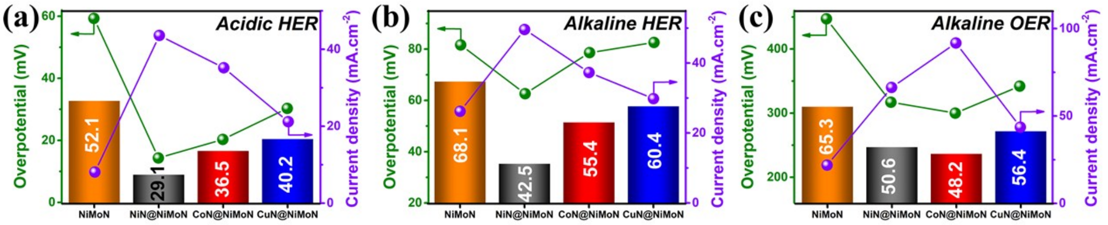

Figure S9. The overpotential for driving a current density of 10 mA cm^{-2}, the current density at 50 mV versus RHE and the corresponding Tafel plots of all above catalysts for acidic HER (a). The overpotential for driving a current density of 10 mA cm^{-2}, the current density at 150 mV versus RHE and the corresponding Tafel plots of all above catalysts for alkaline HER (b). The overpotential for driving a current density of 50 mA cm^{-2}, the current density at 350 mV versus RHE and the corresponding Tafel plots of all above catalysts for alkaline OER (c).

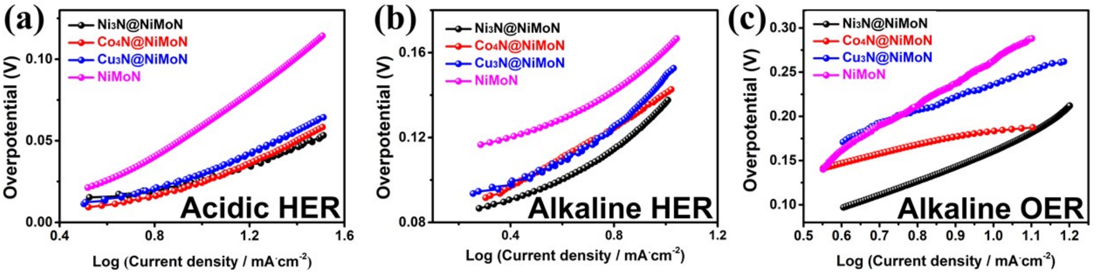

Figure S10. The Tafel plots derived from Figure 3a, 3b.

Note that the data were modified by iR-loss correction. Linear portions of Tafel plots under a small overpotential were fitted to the Tafel equation ($\eta = b \log j + a$, where j is the current density and b is the Tafel slope).

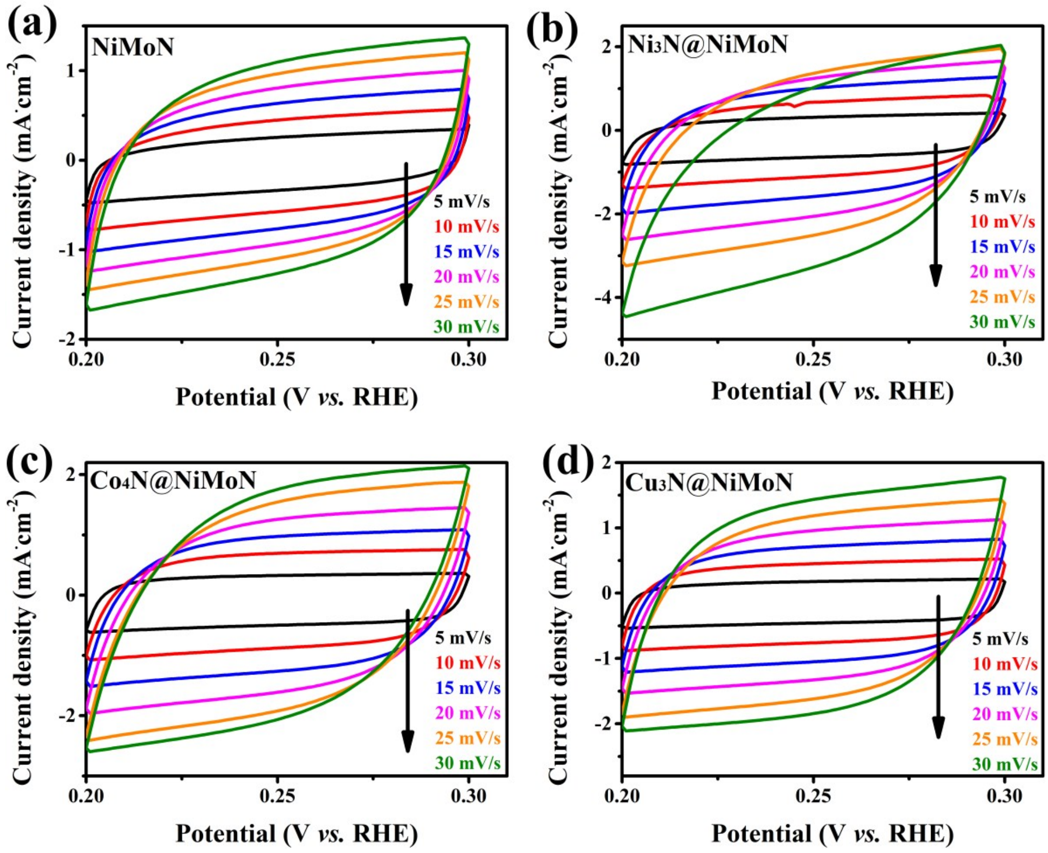

Figure S11. Electrochemical cyclic voltammetry curves at different potential scanning rates for NiMoN (a), Ni_3N@NiMoN (b), Co_4N@NiMoN (c) and Cu_3N@NiMoN (d) electrodes.

The electrochemical C_{dl} for evaluation of the EESA was achieved by a sample CV method.

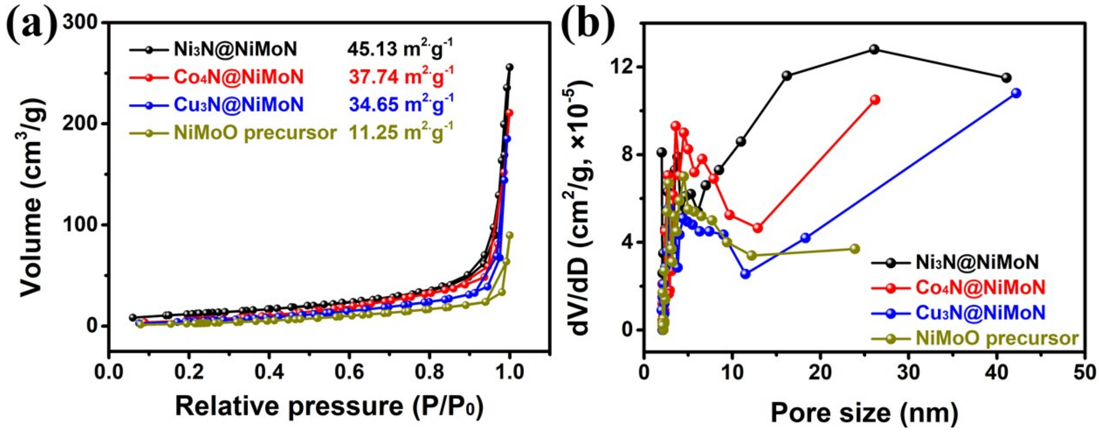

Figure S12. BET surface area of NiMoO precursor, Ni_3N@NiMoN, Co_4N@NiMoN and Cu_3N@NiMoN (a).The corresponding pore size distribution of the as-synthesized specimen above (b).

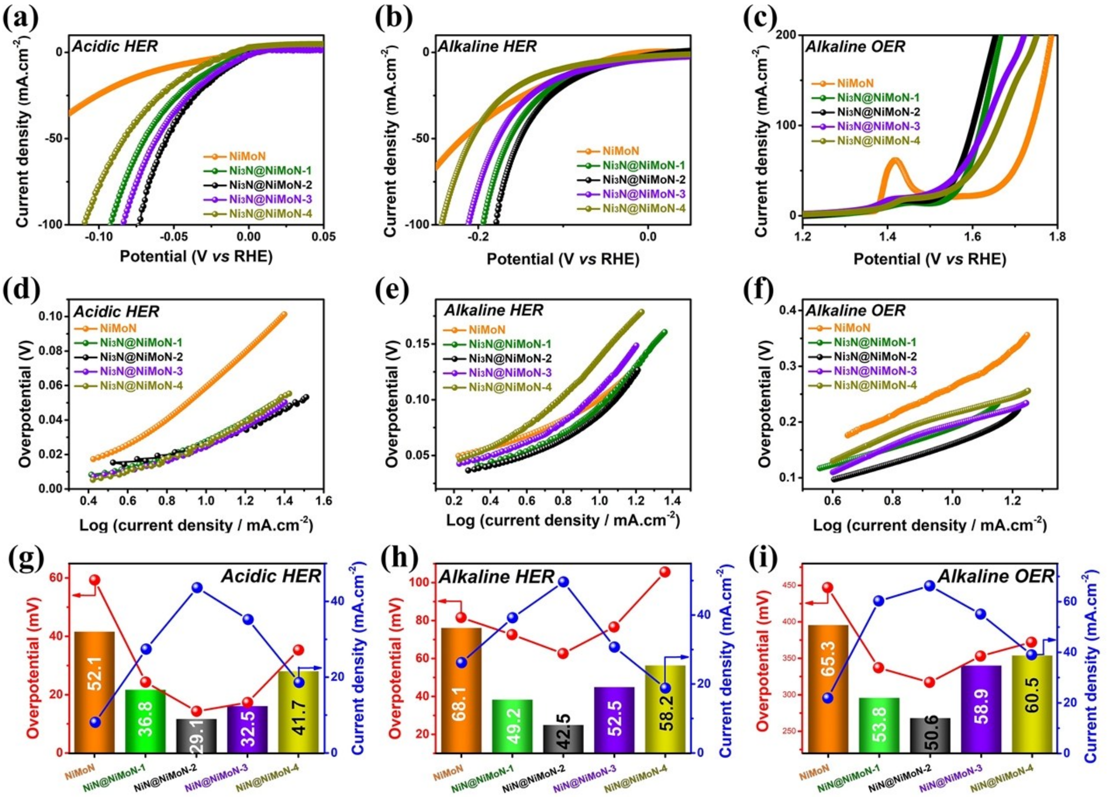

Figure S13. Comparison of acidic HER (a) and alkaline HER(b)/OER(c) polarization curves using NiMoN and Ni_3N@NiMoN-1/2/3/4 heterostructures. (d, e, f) The tafel plots derived from above polarization curves. The overpotential for driving a current density of 10 mA·cm^{-2}, the current density at 50 mV versus RHE and the corresponding Tafel plots of all above catalysts for acidic HER (g). The overpotential for driving a current density of 10 mA·cm^{-2}, the current density at 150 mV versus RHE and the corresponding Tafel plots of all above catalysts for alkaline HER (h). The overpotential for driving a current density of 50 mA·cm^{-2}, the current density at 350 mV versus RHE and the corresponding Tafel plots of all above catalysts for alkaline OER (i).

Clearly, Ni_3N@NiMoN-2 displays the best acidic HER catalytic performance, with an operating potential of 14.3 mV at the current density of 10 mA·cm^{-2} and a high current density of 43.6 mA·cm^{-2} at the overpotential of 50 mV (**Figures S12a, g**). The polarization curves also show that the overpotentials needed for NiMoN and Ni_3N@NiMoN-1/3/4 achieving a catalytic current density of 10 mA·cm^{-2} are 59.3, 24.3, 17.3 and 35.3 mV, respectively (**Figure S12a**). Accordingly, the current density at 50 mV of NiMoN and Ni_3N@NiMoN-1/3/4 are 8.1, 27.4, 35.2 and 18.6 $mA{\cdot}cm^{-2}$, respectively (**Figure S12g**). The fitted Tafel plot for Ni_3N@NiMoN-2 shows a Tafel slope of 29.1 mV/dec, which acts superior to the single NiMoN (52.1 mV/dec) and Ni_3N@NiMoN-1/3/4 (36.8, 32.5 and 41.7 mV/dec) (**Figures S12d, g**). To drive the current density of 10 $mA{\cdot}cm^{-2}$ for alkaline HER, NiMoN and Ni_3N@NiMoN-1/2/3/4 require 81.6, 72.6, 62.6 mV, 76.6 mV and 105.6 mV, respectively (**Figures S12b, h**). In addition, the current density at 150 mV of NiMoN and Ni_3N@NiMoN-1/2/3/4 are 26.2, 39.2, 49.6, 30.7 and 18.8 $mA{\cdot}cm^{-2}$ (**Figures S12b, h**). The overpotential at 50 $mA{\cdot}cm^{-2}$ gradually decrease from 317 to 372 mV and the current density drove by 350 mV increase from 39.0 to 66.3 $mA{\cdot}cm^{-2}$ implying an initial enhanced OER activity with the introduction of Ni_3N component (**Figures S12c, f, i**).

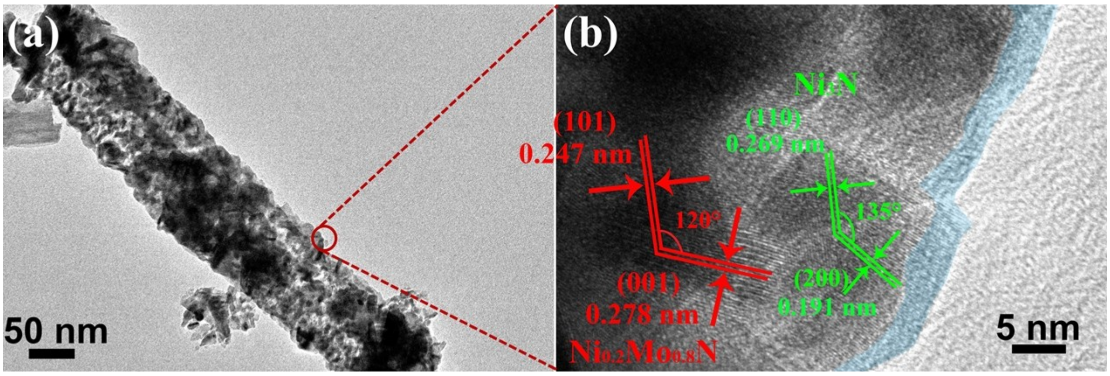

Figure S14. HRTEM image of Ni_3N@NiMoN after OER.

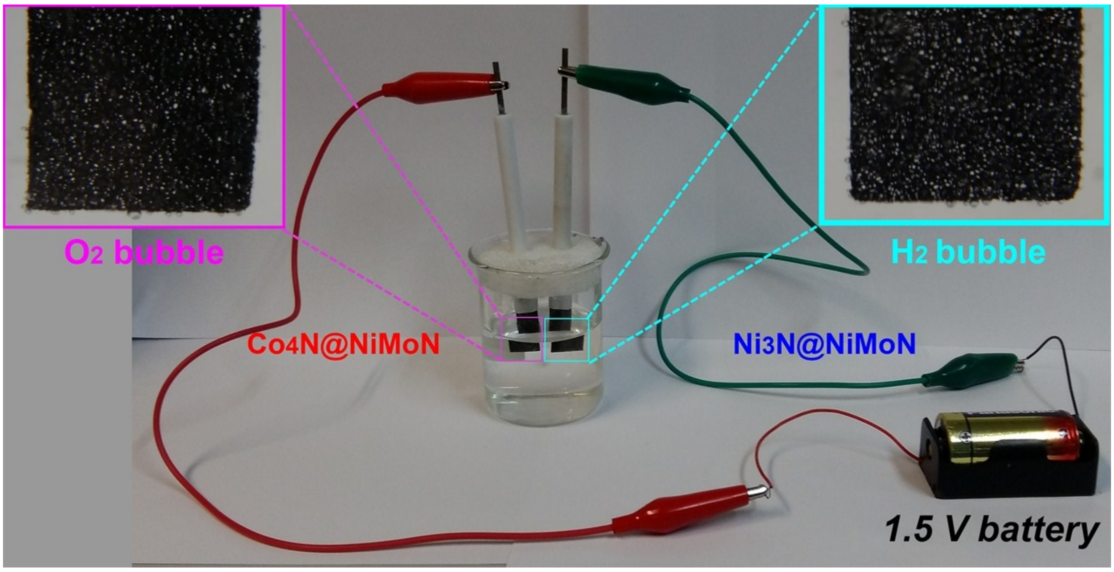

Figure S15. A photograph of overall water splitting on Co_4N@NiMoN/ Ni_3N@NiMoN electrodes in a two-electrode setup driven by a 1.5 V battery.

S5. Supplementary Table

Table S1. The elements contents from EDS measurement of M_xN@NiMoN (M=Ni, Co and Cu) composites.

Sample	Ni_3N@NiMoN		Co_4N@NiMoN		Cu_3N@NiMoN	
	Weight%	Atomic%	Weight%	Atomic%	Weight%	Atomic%
N K	13.2	44.32	14.42	45.97	10.17	34.22
Mo L	44.6	21.86	48.20	22.04	34.44	20.63
Ni K	42.2	33.81	32.08	24.44	42.35	33.35
M K	-	-	5.31	4.03	13.03	11.79
Totals	100		100		100	

Table S2. Bifunctional electrocatalyst for overall water splitting in 1.0 M KOH solution.

Catalysts (Cathode (H_2))	**Catalysts (Anode (O_2))**	**Potential (V) at 10 mA·cm^{-2}**	**References**
Ni_3N@NiMoN	**Co_4N@NiMoN**	**1.481**	**This work**
Ni_3N@NiMoN	**Ni_3N@NiMoN**	**1.517**	
Co_4N@NiMoN	**Co_4N@NiMoN**	**1.553**	
Cu_3N@NiMoN	**Cu_3N@NiMoN**	**1.552**	
Pt/C	Pt/C	1.83	*Nat. Commun.*, **2013**, 4, 2390 [7]
Pt/C	IrO_2	1.71	
NiFe LDH@NiCoP	NiFe LDH@NiCoP	1.57	*Adv. Funct. Mater.*, **2018**, 28, 1706847 [8]
CoP@NCNHP	CoP@NCNHP	1.64	*J. Am. Chem. Soc.*, **2018**, 140, 2610 [9]
$Fe_{0.09}Co_{0.13}$@$NiSe_2$	$Fe_{0.09}Co_{0.13}$@$NiSe_2$	1.52	*Adv. Mater.*, **2018**, 1802121 [10]
Ni_2P nanoparticles	Ni_2P nanoparticles	1.63	*Energy Environ. Sci.*, **2015**, 8, 2347 [11]
NiFe@$NiCo_2O_4$	NiFe@$NiCo_2O_4$	1.67	*Adv. Funct. Mater.*, **2016**, 26, 3515 [12]
Ni@NiP	Ni@NiP	1.56	*Adv. Funct. Mater.*, **2016**, 26, 3314 [13]
CoMnCH nanosheets	CoMnCH nanosheets	1.68	*J. Am. Chem. Soc.*, **2017**, 139, 8320 [14]
$Co_5Mo_{1.0}O$ nanosheets	$Co_5Mo_{1.0}P$ nanosheets	1.68	*Nano Energy*, **2018**, 45, 448 [15]
$Ni_{0.33}Co_{0.67}S_2$	$NiCoO_4$	1.73	*Adv. Energy Mater.*, **2015**, 5, 1402031 [16]

Co_3Se_4 nanowires	Co_3Se_4 nanowires	1.59	*Adv. Energy Mater.*, **2017**, 1602579 [17]

Supplementary References

[1] B. Chang, J. Yang, Y. L. Shao, L. Zhang, W. L. Fan, B. B. Huang, Y. Z. Wu, X. P. Hao, *ChemSusChem* **2018**, 11, 3198.

[2] J. Zhang, T. Wang, P. Liu, Z. Q. Liao, S. H. Liu, X. D. Zhuang, M. W. Chen, E. Zschech, X. L. Feng, *Nat. Commun.* **2017**, *8*, 15437.

[3] S. H. Cho, K. R. Yoon, K. Shin, J. W. Jung, C. Kim, J. Y. Cheong, D. Y. Youn, S. W. Song, G. Henkelman, I. D. Kim, *Chem. Mater.* **2018**, 30, 5941.

[4] Y. Z. Li, T. T. Li, W. Chen, Y. Y. Song, *ACS Appl. Mater. Interfaces* **2017**, 9, 29881-29888.

[5] S. Mondal, C. R. Raj, *J. Phys. Chem. C*, **2018**, 122, 18468.

[6] L. C. Wang, B. H. Liu, C. Y. Su, W. S. Liu, C. C. Kei, K. W. Wang, T. P. Perng, *ACS Appl. Nano Mater.* **2018**, 1, 3673.

[7] H. T. Wang, H. W. Lee, Y. Deng, Z. Y. Lu, P. C. Hsu, Y. Y. Liu, D. C. Lin, Y. Cui, *Nat. Commun.* **2015**, 6, 7261.

[8] H. J. Zhang, X. P. Li, A. Hähnel, V. Naumann, C. Lin, S. Azimi, S. L. Schweizer, A. W. Maijenburg, R. B. Wehrspohn, *Adv. Funct. Mater.* **2018**, 28, 1706847.

[9] Y. Pan, K. A. Sun, S. J. Liu, X. Cao, K. L. Wu, W. C. Cheong, Z. Chen, Y. Wang, Y. Li, Y. Q. Liu, D. S. Wang, Q. Peng, C. Chen, Y. D. Li, *J. Am. Chem. Soc.* **2018**, 140, 2610.

[10] Y. Q. Sun, K. Xu, Z. X. Wei, H. L. Li, T. Zhang, X. Y. Li, W. P. Cai, J. M. Ma, H. J. Fan, Y. Li, *Adv. Mater.* **2018**, 1802121.

[11] L. A. Stern, L. G. Feng, F. Song, X. L. Hu, *Energy Environ. Sci.* **2015**, 8, 2347.

[12] C. L. Xiao, Y. B. Li, X. Y. Lu, C. Zhao, *Adv. Funct. Mater.* **2016**, 26, 3515.

[13] G. F. Chen, T. Y. Ma, Z. Q. Liu, N. Li, Y. Z. Su, K. Davey, S. Z. Qiao, *Adv. Funct. Mater.* **2016**, 26, 3314.

[14] T. Tang, W. J. Jiang, S. Niu, N. Liu, H. Luo, Y. Y. Chen, S. F. Jin, F. Gao, L. J.

Wan, J. S. Hu, *J. Am. Chem. Soc.* **2017**, 139, 8320.

[15] Y. Zhang, Q. Shao, S. Long, X. Q. Huang, *Nano Energy* **2018**, 45, 448.

[16] Z. Peng, D. Jia, A. A. Enizi, A. A. Elzatahry, G. F. Zheng, *Adv. Energy Mater.* **2015**, 5, 1402031.

[17] W. Li, X. F. Gao, D. H. Xiong, F. Wei, W. G. Song, J. Y. Xu, L. F. Liu, *Adv. Energy Mater.* **2017**, 1602579.